Chinese Chemical Letters 37 (2026) 111629

Contents lists available at ScienceDirect

Chinese Chemical Letters

journal homepage: www.elsevier.com/locate/cclet

Atropisomeric carbon-rich macrocycles: Synthesis, structural evolution, and properties

Ke-Lin Zhu, Zhi-Ao Li, Jiaqi Liang, Yong He*, Han-Yuan Gong*

College of Chemistry, Beijing Normal University, Beijing 100875, China

ARTICLE INFO

Article history:
Received 9 May 2025
Revised 4 July 2025
Accepted 22 July 2025
Available online 24 July 2025

Keywords:
Atropisomer
Carbon-rich macrocycles
Supramolecular assembly
Host-guest chemistry
Stimulus responsive materials

ABSTRACT

Carbon-rich cycloarene macrocycles can adopt multiple atropisomeric forms due to steric hindrance restricting σ-bond rotation. These distinct conformations exhibit variations in cavity structure, electronic properties, and functional site distribution, leading to diverse molecular recognition and self-assembly behaviors. In recent years, research on carbon-rich cycloarene macrocyclic compounds has emerged as a cutting-edge and interdisciplinary focus in the fields of carbon-rich functional molecules and macrocyclic chemistry. This review provides a comprehensive overview of the development of atropisomers in carbon-rich cycloarene macrocycles, spanning their design and synthesis, optoelectronic properties, and supramolecular chemistry.

© 2025 Published by Elsevier B.V. on behalf of Chinese Chemical Society and Institute of Materia Medica, Chinese Academy of Medical Sciences.

1. Introduction

In recent decades, carbon-rich macrocycles, whose backbones are composed exclusively of sp^2– and/or sp-hybridized carbon atoms, have emerged as structurally versatile platforms in supramolecular chemistry. Their unique electronic properties and rigid π-conjugated frameworks enable precise spatial arrangement and strong intermolecular interactions, making them attractive candidates for the development of advanced materials [1–7]. In parallel, atropisomerism, a phenomenon arising from the restricted rotation around σ bonds, has gained significant attention in chemistry. Molecules exhibiting atropisomerism can adopt stable stereoisomeric forms due to steric hindrance, which can be exploited to modulate molecular recognition, assembly behavior, and chiral functionality. Representative examples include calix[4]arenes and pillararenes, which can be locked into specific conformations through the strategic introduction of bulky substituents [8–13]. Each atropisomer exhibits unique cavity structures and functional site distributions, resulting in diverse molecular recognition and self-assembly behaviors [14–34].

In contrast to the extensively studied conventional macrocyclic systems, the rotational isomers of carbon-rich aromatic macrocycles represent a distinct and underexplored class of compounds with unique scientific significance. On the one hand, these systems serve as a conceptual bridge between traditional macrocyclic chemistry and the field of dynamic stereochemistry, offering new perspectives on conformational control and molecular motion. On the other hand, the ability to modulate their conformational dynamics provides a powerful means to influence key functional properties, including optoelectronic behavior, host–guest recognition, and chiroptical responses. These characteristics highlight the potential of controlling macrocyclic atropisomerism as promising strategies for the development of stimuli-responsive smart materials. However, the research on the atropisomerism of carbon-rich cycloarene macrocycles remains underexplored and is still in its early developmental stages. This is primarily due to their intricate topological structures, which present significant challenges in understanding their transformation mechanisms and developing precise regulation strategies.

Herein, this review is structured into three main sections, providing a comprehensive discussion of recent advances in the study of enantiotropic and non-enantiotropic atropisomerism in carbon-rich cycloarene macrocycles. These macrocycles, such as cyclo[*n*]paraphenylenes and nanobelts, atropisomerism typically originates from conformational restrictions associated with twisted or folded π-conjugated frameworks. These topological distortions lead to significant hindrance in bond rotation, particularly when the macrocycle is fused with sterically demanding aromatic subunits (*e.g.*, chrysene) or bears bulky substituents near the bridging positions between adjacent aromatic rings. Such steric and geometric constraints stabilize distinct atropisomeric conformations, rendering them isolable and functionally tunable. Specifically, this review covers key aspects including synthesis, structural characteristics, optical and coordination properties, supramolecular behav-

* Corresponding authors.
E-mail addresses: heyong@bnu.edu.cn (Y. He), hanyuangong@bnu.edu.cn (H.-Y. Gong).

https://doi.org/10.1016/j.cclet.2025.111629
1001-8417/© 2025 Published by Elsevier B.V. on behalf of Chinese Chemical Society and Institute of Materia Medica, Chinese Academy of Medical Sciences.

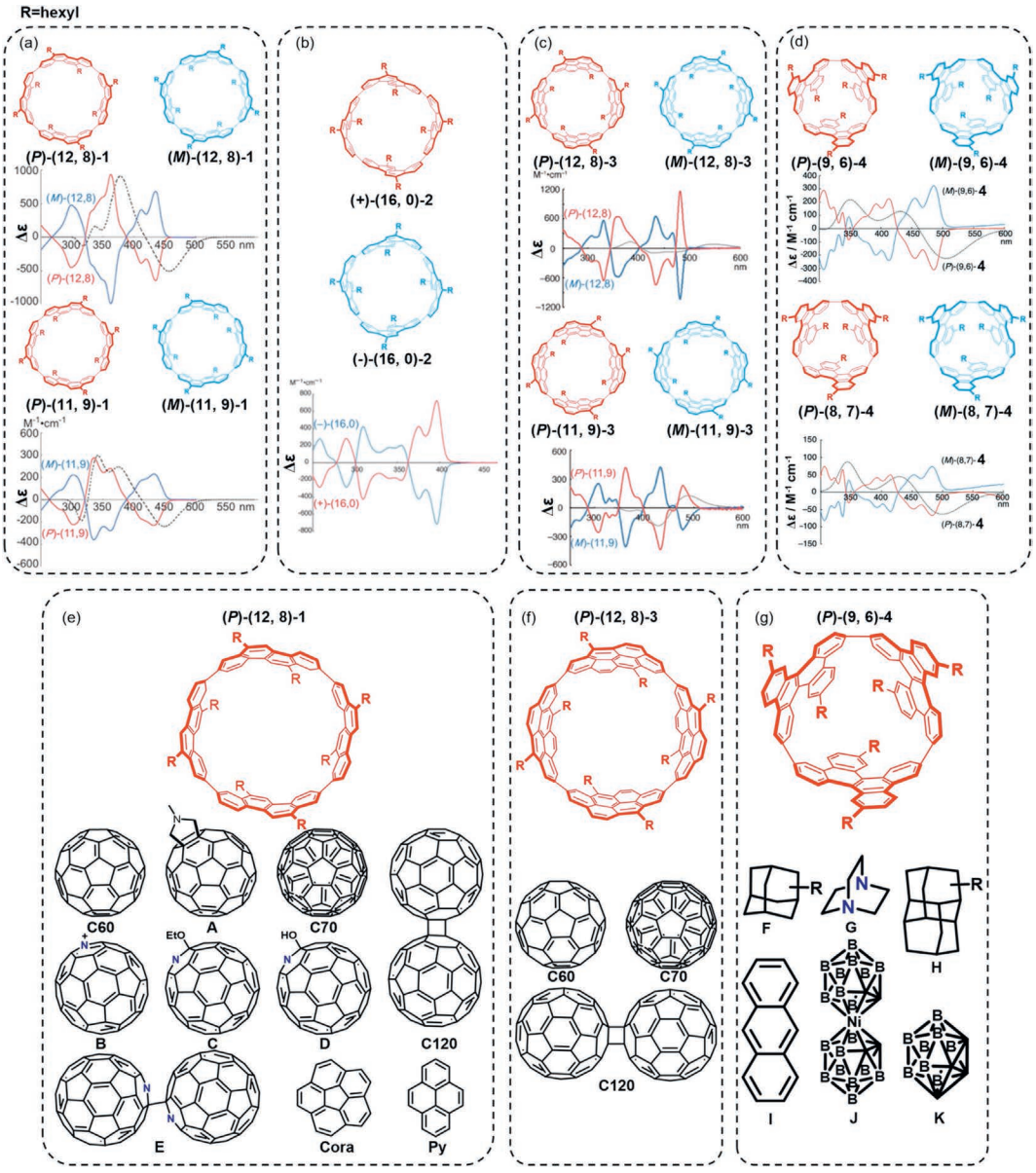


Fig. 1. A series of chiral carbon-rich macrocycles incorporating chrysene motifs and their circular dichroism (CD) spectra: (a) (12,8)-**1** and (11,9)-**1**; (b) (16,0)-**2**; (c) (12,8)-**3** and (11,9)-**3**; (d) (9,6)-**4** and (8,7)-**4**. Representative guest molecules exhibiting notable host–guest interactions with macrocycles: (e) (12,8)-**1**, (f) (12,8)-**3**, and (g) (9,6)-**4**. Adapted with permission [32–35]. Copyright 2011, Springer Nature Limited; Copyright 2012, American Chemical Society; Copyright 2013, The Royal Society of Chemistry; and Copyright 2019, Wiley-VCH Verlag GmbH & Co. KGaA.

ior, and potential applications. Furthermore, it highlights the necessity of future research efforts in molecular design, structure-activity relationship analysis, and the development of stimulus-responsive self-assembly systems. Emphasis is placed on advancing precise regulation strategies and promoting the application of high-performance materials.

2. Enantiotropic atropisomers of carbon-rich cycloarene macrocycles

2.1. Enantiotropic atropisomers in carbon-rich cycloarenes featuring a single macrocyclic framework

Atropisomerization-based design is an effective strategy for the generation of chiral carbon-rich cycloarene macrocycles. In 2011, Isobe's group employed a bottom-up approach to synthesize macrocycle **1** using 2,8-dibromochrysene as a building block, establishing a constrained model for helical (n,m)-single-walled carbon nanotubes (SWNTs) [35]. High-performance liquid chromatography (HPLC) enabled the successful separation of all rotational isomers of macrocycle **1**. Among them, the (12,8)-**1** and (11,9)-**1** isomers were further resolved into their enantiomers, (*P*)- and (*M*)-forms, using chiral HPLC, and their chiral properties were characterized by CD spectroscopy (Fig. 1a). Notably, this study revealed a stereochemical bias during the synthesis: when excess cholesteryl stearate was employed in the reductive elimination step, the resulting macrocycle **1** showed preferential formation of (*P*)-isomers over (*M*)-isomers, with enantiomeric excesses (*ee*) of 17 % for (12,8)-**1** and 11 % for (11,9)-**1**. This asymmetric induction phenomenon offers valuable insight for the future design of stereoselective synthetic strategies. Over the past decade, Isobe and co-workers have reported a series of structurally defined, chiral carbon-rich macrocycles (**2**–**4**) derived from chrysene units *via* platinum-mediated cyclization [36–38]. Several of these molecules,

such as (16,0)-**2**, (12,8)-**3**, (11,9)-**3**, (9,6)-**4**, and (8,7)-**4**, exhibited distinct atropisomeric conformations. Their enantiomers were successfully separated using chiral HPLC and their chiroptical properties were confirmed by CD spectroscopy (Figs. 1b–d).

Among these, (12,8)-**1** displayed particularly rich supramolecular behavior. It formed strong CH–π interactions with various guest molecules. In 2013, it was demonstrated that (12,8)-**1** can co-crystallize with C_{60} to form a solid-state rotor that undergoes processional and spinning motions at different temperatures. Functionalization of C_{60} to produce *N*-methyl fulleropyrrolidine (guest A) enabled the design of a uniaxially molecular rotators bearing (12,8)-**1** [39]. Subsequent studies showed that (12,8)-**1** also encapsulates nitrogen-containing C_{60} derivatives (guests B–E) in stable complexes [40]. Additionally, (12,8)-**1** formed stable complexes with C_{70}, with a binding constant of log $K_a = 9.5$, comparable to that of C_{60} (log$K_a = 9.6$), indicating similar affinity [41].

The host–guest complexation extended to the dumbbell-shaped dimer [60]fullerene (C_{120}), where (12,8)-**1** spontaneously formed a 2:1 supramolecular assembly through a two-step binding process. The corresponding association constants were log$K_{a1} = 11.9$ and log$K_{a1} = 8.0$, with a Gibbs free energy difference (ΔG) of 5 kcal/mol between the two steps [42]. Beyond spherical fullerenes, (12,8)-**1** also interacted with planar and bowl-shaped guests. For instance, it formed both 1:1 and 1:2 complexes with corannulene (Cora), where the K_a for the 1:1 complex was 2.94×10^3 L/mol. Single-crystal X-ray diffraction confirmed the 1:2 complex, wherein weak hydrogen bonding facilitated ultrafast guest rotation within the host at gigahertz frequencies [43]. In contrast, binding with the more planar and elliptical guest pyrene (Py) yielded weaker binding ($K_a = 41$–174 L/mol), and the resulting steric constraints significantly inhibited rotational freedom, enabling design of decelerated molecular rotors [44]. This tunable dynamic behavior illustrates a promising strategy for molecular machine design.

Compared to (12,8)-**1**, macrocycle (12,8)-**3** exhibited narrower guest selectivity. It formed complexes with C_{60}, C_{70}, and C_{120}, with similar binding affinities: log$K_a = 9.7$ for C_{60} and 9.6 for C_{70}. The stepwise binding with C_{120} yielded log$K_{a1} = 9.2$ and log$K_{a2} = 5.7$, both lower than those observed for (12,8)-**1** [41,45]. Owing to its deeper cavity, (12,8)-**3** promoted the formation of ratchet-like host–guest systems with reduced rotational disorder. Experimental and theoretical investigations have since explored the dynamic motions within these complexes [46–48].

In contrast, macrocycle (9,6)-**4** exhibited unique host–guest behavior, forming CH–π complexes with guests containing sp^3- and sp^2-hybridized carbon centers (guests F–K) [49]. These complexes displayed moderate binding affinities ($K_a = 110$–183 L/mol) and spontaneously assembled into exfoliable, layered two-dimensional (2D) honeycomb crystals, enabling centimeter-scale single-crystal growth. Recent studies have further elucidated the dynamic behavior of these assemblies using both experimental techniques and computational modeling [50,51].

In 2011, Itami's group synthesized the chiral molecule **5** ([13]CPPN) by incorporating a naphthalene unit into cycloparaphenylenes (CPPs) using a [7 + 7] fragment coupling Strategy (Fig. 2a) [52]. However, due to its low racemization barrier (8.4 kcal/mol), a pair of enantiomers separation was not feasible at room temperature (Fig. 2b). Computational studies further revealed that reducing the number of benzene units or increasing the number of acene units would elevate the racemization barrier. These findings suggest that such nanorings have the potential to form stable chiral molecules, providing both experimental and theoretical foundations for future molecular design.

Since 2019, Du's group has synthesized chiral CPPs **6** [53], **7a**–**c** [54], and **8** [55] by incorporating naphthalene or anthracene fragments as structural units (Fig. 3a). Compounds **7a**, **7b**, and **8** were successfully resolved into their enantiomers by chiral HPLC at

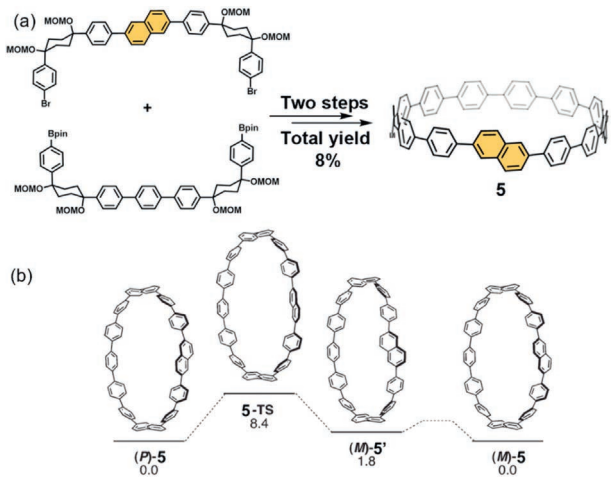


Fig. 2. (a) Synthetic strategy for the preparation of chiral macrocycle **5**. (b) Racemization pathway from (*P*)-**5** to (*M*)-**5**, with the corresponding activation energy ($\Delta G^{\ddagger}$, kcal/mol). Reproduced with permission [52]. Copyright 2011, American Chemical Society.

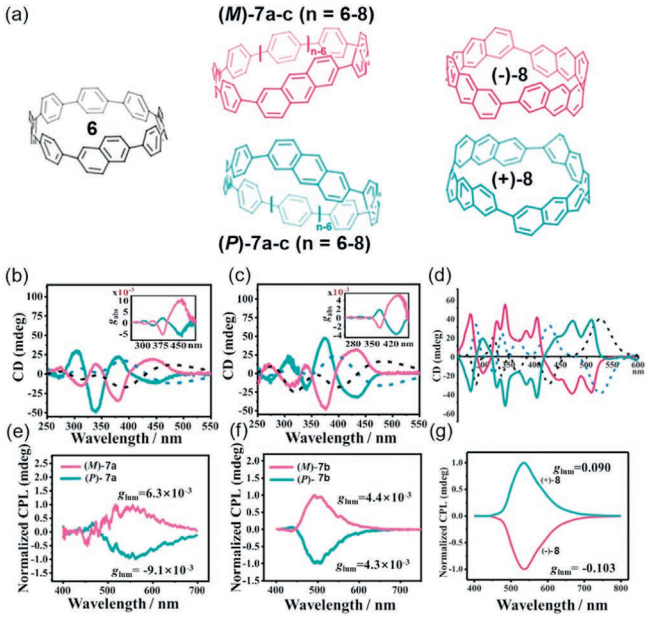


Fig. 3. (a) A series of cycloparaphenylenes (CPPs) (**6**, **7a**-**c**, **8**) incorporating naphthalene or anthracene fragments. (b-d) Circular dichroism (CD) spectrum of (*P*/*M*)-**7a**, (*P*/*M*)-**7b** and (±)-**8**, respectively. (e-g) Circularly polarized luminescence (CPL) spectra of (*P*/*M*)-**7a**, (*P*/*M*)-**7b** and (±)-**8**, respectively. Reproduced with permission [54,55]. Copyright 2022, Wiley-VCH GmbH. Copyright 2020, Wiley-VCH Verlag GmbH & Co. KGaA.

room temperature and exhibited strong chiral signals in both circular dichroism (CD) and circularly polarized luminescence (CPL) spectra (Figs. 3b–g). Notably, compound **8** displayed an exceptionally high luminescence asymmetry factor ($|g_{lum}|$) up to 0.10, demonstrating excellent chiral luminescence properties. The high magnitude of $|g_{lum}|$ observed in this system offers valuable insights for the rational design of next-generation chiral luminescent materials. However, the host–guest recognition properties of this series of macrocycles remain largely unexplored, representing a promising direction for future research.

In 2021, Esser's team reported diketone [*n*]CPPs (**9a**, $n = 6$; **9b**, $n = 7$) and DBP[*n*]CPPs (**10a**, $n = 6$; **10b**, $n = 7$) with diketone core (Fig. 4a) [56]. The UV–vis absorption and fluorescence emission spectra of **9a** and **9b** were highly similar, as were those of **10a** and

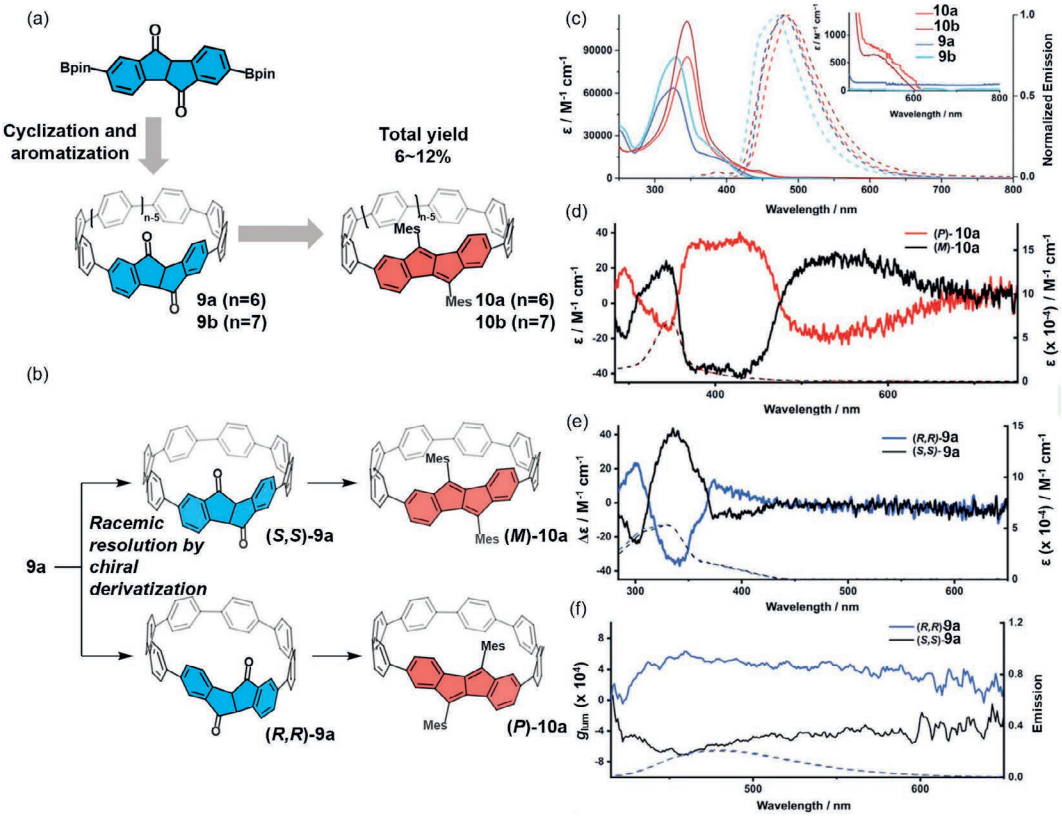


Fig. 4. (a) Synthetic strategy for diketone-functionalized [*n*]cyclopara phenylenes (CPPs) **9a** ($n=6$) and **9b** ($n=7$), as well as dibenzo[*a*,*e*]pentalene-embedded [*n*]CPPs (DBP[*n*]CPPs) **10a** ($n=6$) and **10b** ($n=7$). (b) A pair of enantiomers resolution of **9a** through chiral derivatization of the carbonyl groups to access enantiopure nanohoops **10**. (c) Absorption (10^{-5} to 10^{-6} mol/L) and emission spectra (10^{-6} to 10^{-7} mol/L) of **9a-b** and **10a-b** in CH_2Cl_2. (d) CD spectra of (*P*/*M*)-**10a**. (e) CD spectrum of (*R*,*R*/*S*,*S*)-**9a**. (f) CPL spectra of (*R*,*R*/*S*,*S*)-**9a**. Reproduced with permission [56]. Copyright 2021, The Royal Society of Chemistry.

10b Notably, DBP[*n*]CPPs (**10a** and **10b**) exhibited a slight red shift in both spectra compared to diketone [*n*]CPPs (**9a** and **9b**) (Fig. 4c). Moreover, the authors successfully resolved a pair of enantiomers of **9a** *via* chiral derivatization, achieving an enantiomeric excess (*ee*) up to 99% (Fig. 4b). The chiroptical properties of the resolved enantiomers were further characterized using CD and CPL spectroscopy (Figs. 4c–f). Compound **9a** exhibited a high fluorescence quantum yield ($\Phi_F = 57\%$) with a $|g_{lum}|$ value of approximately 4×10^{-4} at its emission peak. This synthetic strategy enables the scalable production of enantiomerically pure nanohoops, thereby facilitating their integration into advanced applications across materials science and chirality research.

In the same year, Esser's group enantioselectively synthesized the chiral conjugated nanohoop **11** from enantiopure precursors (*R*-/*S*-diketone) and characterized its chiroptical properties [57]. CD spectroscopy revealed a pronounced Cotton effect across the 300–700 nm range (Fig. 5), confirming its strong chiral response. Nanohoop **11**, characterized by its cyclic geometry and extended π-conjugated surface, is particularly well-suited for encapsulating guest molecules such as C_{60}. NMR titration experiments combined with DFT calculations reveal that nanohoop **11** is capable of binding up to two C_{60} molecules, with K_a in the range of 10^2–10^3 L/mol. This binding capacity is attributed to its relatively large internal diameter (~2.5 nm), which accommodates multiple fullerene units.

In recent years, BINOL-derived macrocycles have also been reported, showing their unique optoelectronic properties and host-guest characteristics [58]. In 2022, Cai's group reported the synthesis of a flexible tubular macrocycle (**12**) exhibiting five-fold symmetry, constructed from 4,4′-dimethoxybiphenyl building blocks (Fig. 6a) [59]. Macrocycle **12** features a fully conjugated backbone and emits strong blue fluorescence with a Φ_F value of

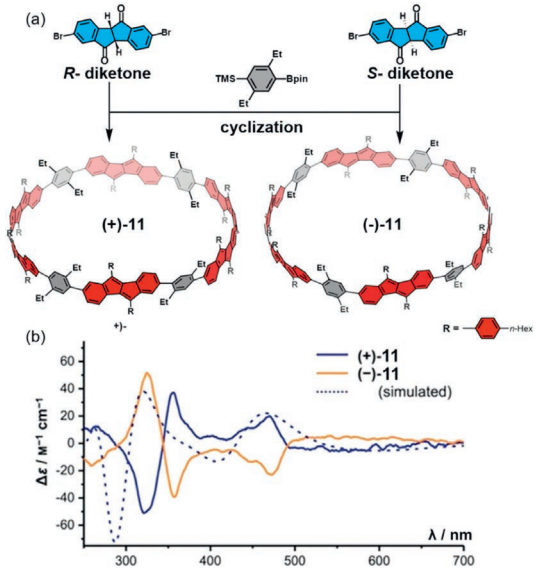


Fig. 5. (a) Schematic representation of the synthesis of nanohoop (±)-**11** *via* macrocyclization of an enantiomerically pure diketone precursor. (b) CD spectra of (±)-**11**. Reproduced with permission [57]. Copyright 2021, The Authors.

56%, indicating its potential for use in luminescent materials and fluorescence-based sensing platforms. The flexible biphenyl segments enable dynamic conformational inversion in solution. Upon addition of chiral guest molecules such as (*S*)-Ga or (*R*)-Ga, **12** exhibits induced CD signals, highlighting its chiral responsiveness

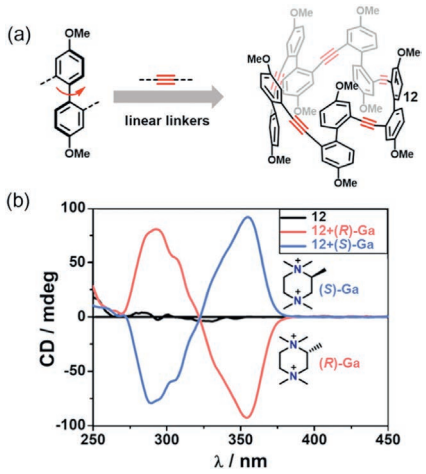


Fig. 6. (a) Synthetic strategy for macrocycle **12**. (b) CD spectra of **12** alone and in the presence of chiral guest molecules (*R*)-Ga and (*S*)-Ga, demonstrating chiroptical responsiveness. Reproduced with permission [59]. Copyright 2022, American Chemical Society.

and potential for enantioselective sensing (Fig. 6b). In the context of host–guest chemistry, macrocycle **12** combines a deep cavity with high conformational adaptability, enabling it to accommodate a wide range of neutral and cationic electron-deficient guests. Its cavity can adapt to diverse molecular geometries, from planar guests like tetracyanoquinodimethane (TCNQ) to spherical fullerenes such as C_{60}, with binding constants spanning from 10^3 L/mol to 10^7 L/mol. Notably, the binding constant with $CoCp_2^+$ reaches 4.79×10^7 L/mol, while that with C_{60} is 2.25×10^4 L/mol. These results underscore the versatility of **12** as a supramolecular host, providing a valuable platform for the development of functional materials. Its modular synthetic strategy and multifunctional properties lay the groundwork for the future design of advanced, functionalized macrocyclic systems.

In 2023, Cai and co-workers reported the synthesis of water-soluble chiral macrocycles *RRRR*/*SSSS*-**13**, constructed from enantiopure 1,1′-bi-2,2′-naphthol (BINOL) precursors (Fig. 7a) [60]. Macrocycle **13** features a conjugated, electron-rich framework with a deep hydrophobic cavity and displays strong fluorescence emission ($\Phi_F = 34\%$) as well as significant CPL in aqueous solution ($|g_{lum}| = 1.4 \times 10^{-3}$) (Figs. 7b and c).

Owing to its structural features, **13** demonstrates excellent binding affinity for hydrophobic, positively charged substrates. Remarkably, it exhibits binding constants up to 10^{10} L/mol for achiral guests and enantioselectivity ratios (K_{SSSS}/K_{RRRR}) of up to 18.7 for chiral analytes, both of which represent benchmark values for chiral macrocycles operating in aqueous environments. The combination of high binding strength, pronounced enantioselectivity, synthetic accessibility, and superior optical activity positions macrocycle **13** as a highly promising candidate for applications in analytical sensing, chiral separation, and molecular recognition.

Building upon their previous design strategies, the same group recently developed a new class of chiral tubular macrocycles, **14a–c** ($n = 3$–5), based on repeating dicarboxylic acid imide units (Fig. 7d) [61]. These molecules exhibit excellent optical properties in nonpolar solvents. In particular, **14a** displays a Φ_F of 75% in cyclohexane. CD and CPL spectroscopic analyses confirmed the presence of strong chiroptical signals across the series, with solvent polarity exerting a notable influence on CPL activity. Notably, **14c** exhibited

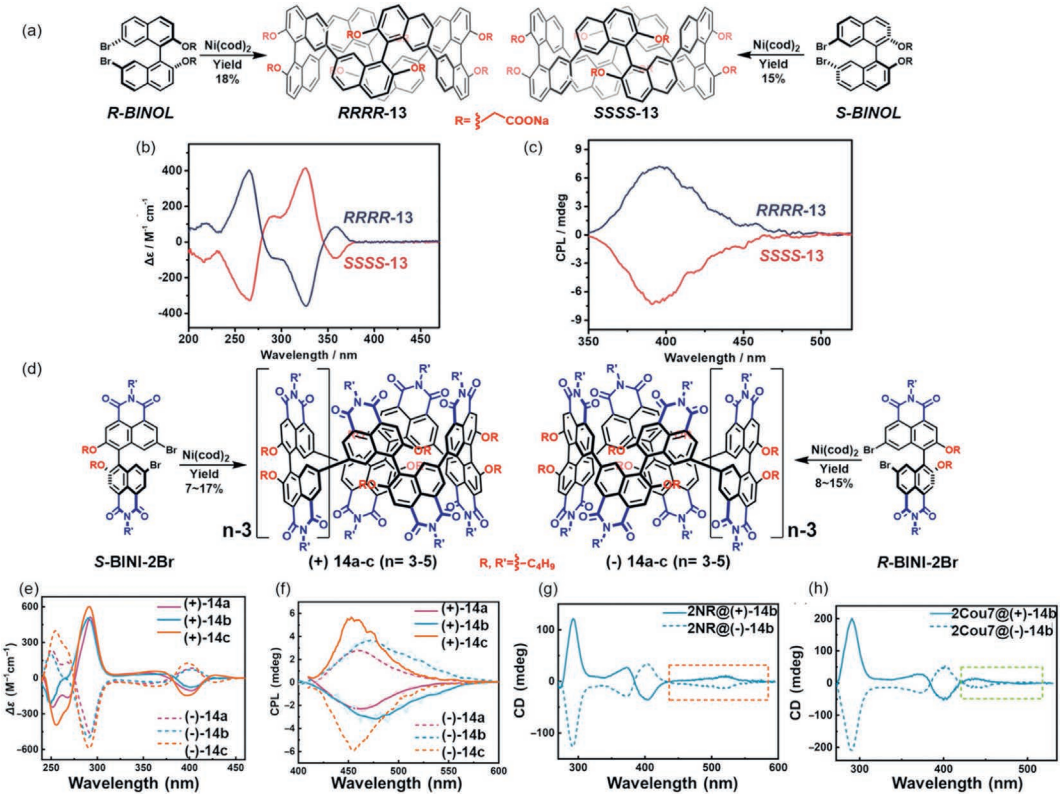


Fig. 7. (a) Synthetic route to water-soluble chiral macrocycles *RRRR*/*SSSS*-**13**. (b) CD spectra of *RRRR*/*SSSS*-**13** in water (2.5×10^{-6} mol/L). (c) CPL spectra of *RRRR*/*SSSS*-**13** in water (2.5×10^{-6} mol/L). (d) Synthetic strategy for tubular chiral macrocycles (±)-**14a–c** ($n = 3$–5). CD (e) and CPL spectra (f) of (+)- and (−)-**14a–c** in $CHCl_3$ (1.0×10^{-5} mol/L). (g) CD spectra of 2NR@(+)-**14b** and 2NR@(−)-**14b** in hexane (**14b**: 40 μmol/L; NR: 80 μmol/L; light path length: 2.0 mm). (h) CD spectra of 2Cou7@(+)-**14b** and 2Cou7@(−)-**14b** in hexane (**14b**: 40 μmol/L; Cou7: 140 μmol/L; light path length: 2.0 mm). Reproduced with permission [60,61]. Copyright 2023, Wiley-VCH GmbH; Copyright 2025, Chinese Chemical Society.

a $|g_{lum}|$ value of 2.4×10^{-3} and a circularly polarized luminescence brightness (B_{CPL}) of 119 L mol^{-1} cm^{-1} for its enantiomer (Figs. 7e and f). Although macrocycles **14a–c** showed lower guest binding affinities ($K_a \approx 10^5$ L/mol) compared to **13**, their supramolecular behavior revealed unique characteristics. For instance, **14b** was capable of simultaneously binding two planar dye molecules, Nile red (NR) and Coumarin 7 (Cou7), in a 1:2 stoichiometry, with a cumulative binding constant of up to 10^{12} M^{-2}. This interaction facilitated chirality transfer from the host to the non-chiral guests, as confirmed by induced CD and CPL signals (Figs. 7g and h). These results suggest that this class of macrocycles can function as effective chiral hosts for modulating the optical activity of bound guests. Future structural modifications, such as the incorporation of hydrophilic substituents, could enable their application in aqueous-phase molecular recognition and artificial transmembrane channel design.

2.2. Enantiotropic atropisomers in carbon-rich cycloarenes featuring a double macrocyclic framework

The enantiotropic atropisomers of cycloarene macrocycles and their derivatives can also adopt bismacrocyclic structures. In 2022, building on the design of SCPP10 [62], Du and colleagues synthesized the chiral dual-state emission bismacrocycle **16** from precursor **15** [63] and successfully resolved its enantiomers *via* chiral HPLC (Fig. 8a). CD spectroscopy revealed that the enantiopure isomer exhibited a $|g_{abs}|$ value of 1.2×10^{-2}, indicating strong chiroptical activity in the ground-state electronic transition (Figs. 8b and c). This pronounced signal is consistent with a high kinetic barrier to racemization, reflecting excellent configurational stability of the atropisomer. In solution, its $|g_{lum}|$ value was 6.9×10^{-3}, while in the aggregated state, the CPL signal was significantly enhanced ($|g_{lum}| = 1.9 \times 10^{-2}$) (Fig. 8d). This enhancement surpasses that observed in many small molecules exhibiting aggregation-induced emission (AIE) properties, highlighting its potential for high-performance chiral optoelectronic applications. However, its host–guest recognition and self-assembly behaviors remain largely unexplored, thereby limiting its further development as a functional supramolecular material.

In 2023, Miao's group reported two negatively curved nanographenes, compound **17** (C_{2V} symmetry) and compound **18** (D_2 symmetry), constructed through the conformationally controlled cyclization of an octabenzo[8]circulene (OB8C) core [64].

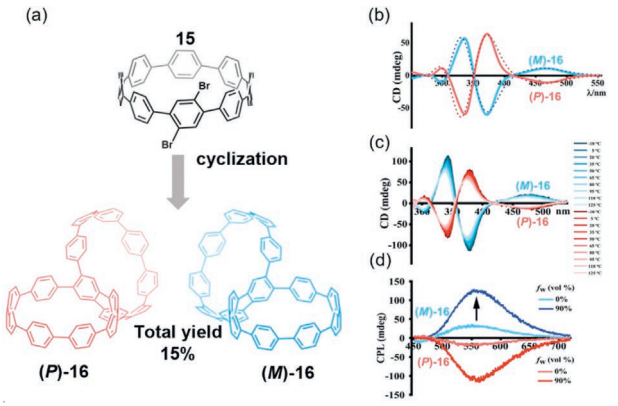


Fig. 8. (a) Synthetic route to chiral macrocycle **16** featuring a 1,2,4,5-tetraphenylbenzene (TPB) core. (b) Experimental (solid lines) and theoretical (dashed lines) CD spectra for (*P*)/(*M*)-**16** in CH_2Cl_2. (c) Temperature-dependent CD spectra of (*P*)/(*M*)-**16** from −10 °C to 125 °C at 15 °C intervals. (d) CPL spectra of (*P*)/(*M*)-**16** in THF solution and in a 90:10 H_2O/THF solution (excited at 355 nm). Reproduced with permission [63]. Copyright 2022, The Author(s).

Their study revealed that the rapid interconversion of two key intermediates significantly contributes to the conformational diversity of the target products (Fig. 9a). Notably, a pair of enantiomers of **18** were successfully separated. Compared to **17**, isomer **18** exhibited a higher molar absorption coefficient and enhanced fluorescence emission intensity (Figs. 9b and c). CD spectroscopy revealed pronounced Cotton effects in the 250–600 nm range (Fig. 9d). Notably, the host–guest recognition behavior of the distinct conformational isomers remains unexplored, leaving a promising direction for future investigation. Overall, this study provides valuable insights into the rational design of multi-conformational nanographenes with negative curvature, highlighting their potential in supramolecular chemistry and molecular recognition.

In 2024, Cong and colleagues synthesized all-carbon conjugated helical nanotubes **20** [65] *via* an axial covalent bonding strategy, using site-specifically functionalized cycloparaphenylene **19** as the building block (Fig. 10a). Compared to [9]CPP, **20** exhibits a significantly higher molar absorption coefficient (Fig. 10b). Especially, **20** demonstrates strong chiral properties, with the circularly polarized luminescence brightness (B_{CPL}) of its enantiomer reaching 1470 L mol^{-1} cm^{-1}, marking one of the highest B_{CPL} values reported for

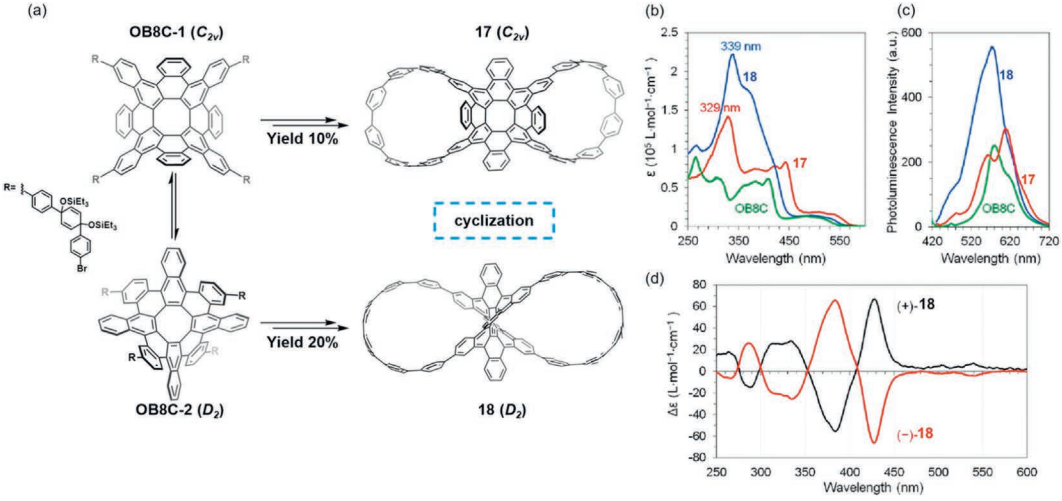


Fig. 9. (a) Curved nanographene **17** and **18** resulting from OB8C precursors with conformational interconversion. (b) UV–vis absorption spectra of **17**, **18**, and OB8C (each concentration as 2.5×10^{-6} mol/L in CH_2Cl_2). (c) Photoluminescence spectra of **17**, **18**, and OB8C (each concentration as 2.5×10^{-6} mol/L in CH_2Cl_2; **17** and **18** excited at 420 nm, OB8C excited at 410 nm). (d) CD spectra of the two enantiomers of **18** (6.0×10^{-5} mol/L in CH_2Cl_2). Reproduced with permission [64]. Copyright 2023, The Authors.

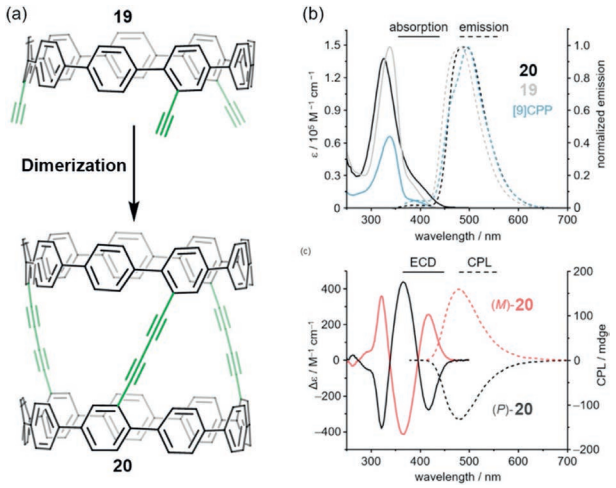


Fig. 10. (a) Helical nanotubes **20** prepared by dimerization of [9]cycloparaphenylene **19**. (b) UV–vis absorption (solid lines) and fluorescence emission (dashed lines) spectra of [9]CPP, **19**, and **20** (5.0×10^{-6} mol/L) in CH_2Cl_2, respectively. (c) electronic circular dichroism (ECD) (solid lines) and CPL (dashed lines) spectra of the enantiomers of **20** (5.0×10^{-6} mol/L in CH_2Cl_2). Reproduced with permission [65]. Copyright 2024, Wiley-VCH GmbH.

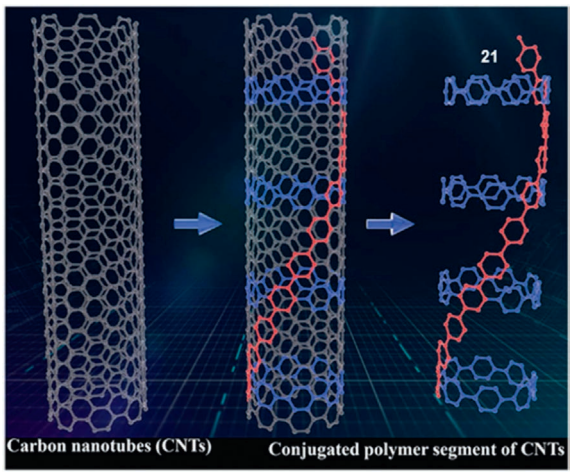


Fig. 11. Design of a long π-extended poly(*para*-phenylene)-based polymeric segment of armchair [8,8]single-walled carbon nanotube **21**. Reproduced with permission [66]. Copyright 2019, American Chemical Society.

chiral organic small molecules (Usually within the order of 10^1–10^2 in organic molecules) (Fig. 10c) [65]. The diacetylene moiety provides a versatile platform for post-synthetic functionalization, enabling the incorporation of additional functional groups or responsive units. However, the potential applications of this system in molecular recognition and artificial channel design remain to be fully explored. Overall, this study presents a novel bottom-up strategy for constructing conjugated nanotubes from cycloparaphenylene (CPP) building blocks, offering new avenues for the development of functional nanostructured materials.

2.3. Enantiotropic atropisomers in carbon-rich cycloarenes featuring a multi macrocyclic framework

Efforts to integrate carbon-rich macrocycles into the construction of chiral carbon materials have recently emerged. In 2019, Du's group reported the first synthesis of long π-conjugated segments of single-chirality single-walled carbon nanotubes (SWCNTs, **21**) *via* one-dimensional nickel-catalyzed polymerization of difunctionalized CPPs (Fig. 11) [66]. This polymer not only exhibits enhanced photophysical properties, including improved absorption and emission characteristics, but also demonstrates efficient charge transport for both electrons and holes. These findings establish a foundation for developing solution-phase synthesis strategies for single-chirality carbon nanotubes.

In 2022, Isobe's group employed triangular phenine units as vertices to construct a minimal chiral cage representing a diamond-twin network (**23**) *via* a coupling reaction [67]. Single-crystal X-ray diffraction analysis confirmed the solid-state structure of compound **23**, while theoretical calculations suggested that it undergoes dynamic chiral inversion in solution. To enhance its stereochemical stability, rigid stereogenic groups were introduced, yielding OMe-**23** (Fig. 12a). This modification enabled chiral resolution, and enantiomerically resolved CD spectra were recorded in the 250–350 nm range (Figs. 12b and c). However, the supramolec-

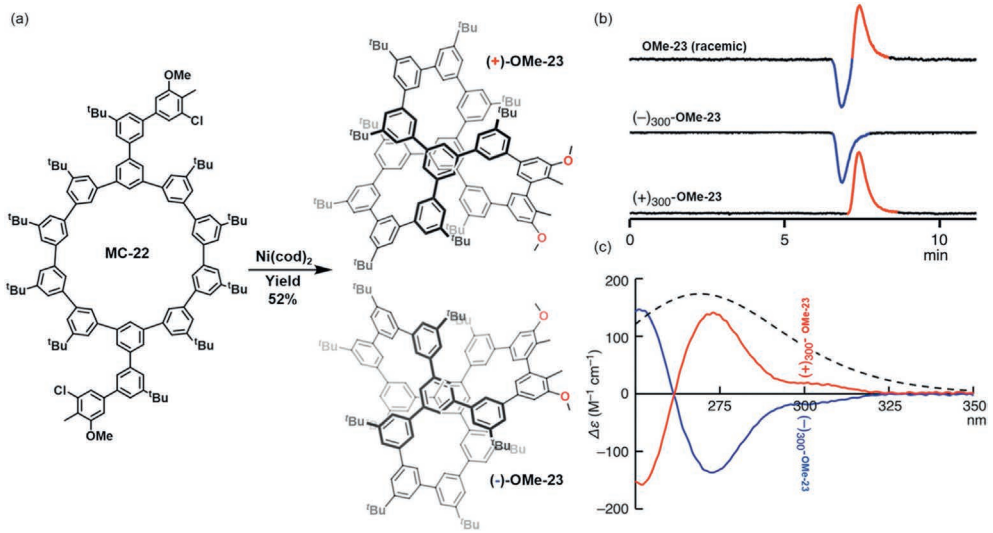


Fig. 12. (a) $Ni(cod)_2$-mediated coupling of macrocycle **MC-22** to form the chiral diamond-twin network (±)-**OMe-23**. (b) Chiral resolution of OMe-**23** using a chiral column (*R*)-1-naphthylglycine (SUMICHIRAL OA-2500, 4.6×250 mm) for chiral HPLC analysis (eluent = 0.5 % 1-butanol/hexane; flow rate = 1.0 mL/min, 40 °C) (stereoisomers are labeled with the CD sign at 300 nm). (c) CD spectra of the enantiomers of OMe-**23** in $CHCl_3$ at 25 °C. Reproduced with permission [67]. Copyright 2022, The Author(s). Published by PNAS.

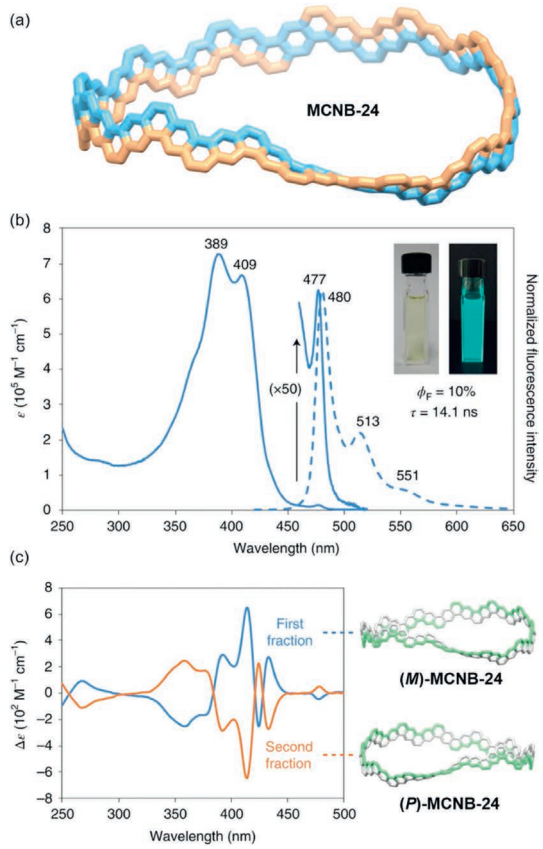


Fig. 13. (a) Molecular structure of Möbius carbon nanobelt **MCNB-24**. (b) UV–vis absorption (solid line) and fluorescence emission (dashed line) spectra of **MCNB-24** in CH_2Cl_2. (c) CD spectra of **MCNB-24** enantiomers in CH_2Cl_2 separated by chiral column chromatography (CHIRALPAK-IE), with tentative assignment of (*M*) and (*P*) configurations. Reproduced with permission from [69]. Copyright 2022, The Author(s), published by Springer Nature.

ular functions of the cavity, such as molecular recognition and guest encapsulation, remain largely unexplored. Nevertheless, this study presents a novel cavity-directed design strategy for constructing chiral carbon-rich materials, offering new opportunities in supramolecular chemistry and functional material development.

On the other hand, carbon-rich macrocycles can also adopt Möbius topologies, leading to inherently chiral spatial configurations. The unique topological features of Möbius macrocycles have garnered significant interest in recent years due to their fundamental and potential functional relevance in molecular design. Research on this molecular architecture has been reviewed and further developed across several studies [68].

In 2022, Itami and co-workers reported the synthesis of a Möbius carbon nanobelt, **MCNB-24** (Fig. 13a), *via* a Z-selective Wittig reaction followed by a nickel-mediated intramolecular homocoupling process [69]. The UV–vis absorption spectrum of **(25,25)MCNB** displayed peaks at 389 and 409 nm, along with a very weak absorption at 477 nm. Fluorescence emission was observed at 480, 513, and 551 nm, with a Φ_F value of 10 % (Fig. 13b). The Möbius topology imparts inherent chirality to the molecule, and its topological enantiomers were separated by chiral HPLC and characterized *via* CD spectroscopy. The two stereoisomers were tentatively assigned as the *P* and *M* enantiomers (Fig. 13c). However, further investigation into additional chiroptical properties and host–guest recognition capabilities of this unique molecular structure was not pursued in this study.

In 2025, Miao and co-workers reported the synthesis of a nanobelt (**25**) featuring a norbornene framework, constructed *via*

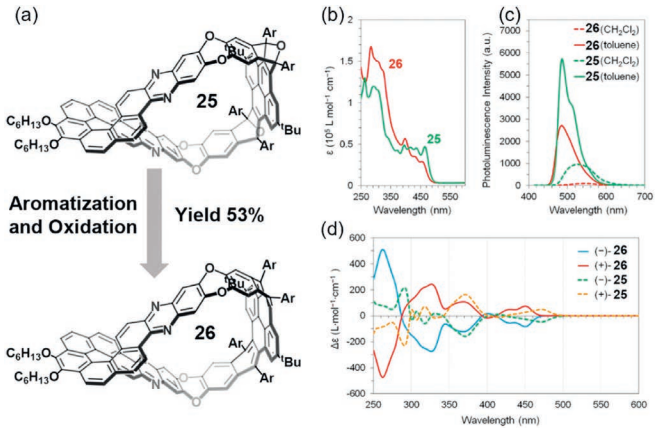


Fig. 14. (a) Synthesis of nanobelt **26** *via* reductive aromatization and oxidation of precursor **25**. (b) UV–vis absorption spectra of **25** and **26** in CH_2Cl_2 (1×10^{-5} mol/L, $\lambda_{ex} = 396$ nm). (c) Photoluminescence spectra of **25** and **26** in CH_2Cl_2 and toluene (1×10^{-5} mol/L). (d) CD spectra of **25** and **26** in CH_2Cl_2. Reproduced with permission [70]. Copyright 2025, American Chemical Society.

aromatic nucleophilic substitution between a helicene-derived unit (based on [7]helicene) and a *C*-shaped segment derived from pyrene [70]. Compound **25** was subsequently converted into a twisted Möbius nanobelt (**26**) through sequential reductive aromatization and DDQ-mediated oxidation (Fig. 14a). The resulting molecule exhibited a writhed topology, which endowed it with unique photophysical characteristics. Both **25** and **26** displayed pronounced sensitivity to solvent polarity, with a Φ_F value of 2.9 % in CH_2Cl_2 and 24.3 % in toluene (Figs. 14b and c). However, these nanobelts were photochemically unstable, undergoing decomposition upon light exposure. Notably, enantiopure **26** could be obtained by employing enantiopure helicene precursors. The compound exhibited strong chiroptical activity, with CD ($|g_{abs}| = 4 \times 10^{-3}$) and CPL ($|g_{lum}| = 1 \times 10^{-3}$), highlighting its potential for chiral photonic applications (Fig. 14d). This work introduces a novel molecular design strategy that expands the toolbox for creating advanced chiral optoelectronic materials based on topologically nontrivial carbon-rich frameworks.

Chiral carbon-rich macrocycles can be constructed by linking aromatic ring moieties and carbon atoms, exhibiting topological or atropisomeric chirality. In recent years, numerous studies have reported the synthesis of various chiral cycloarene macrocycles, including spirobifluorene-based chiral macrocycles and alkyne-linked bismacrocycles, with promising applications in chiral recognition and luminescent materials [71–87]. Moreover, these macrocycles can serve as key intermediates for constructing novel topologically chiral systems, such as figure-8-shaped chiral carbon nanoribbons [88,89], catenanes and rotaxanes [90,91], offering a promising pathway for the structural innovation of carbon-rich materials.

3. Non-enantiotropic atropisomers of carbon-rich cycloarene macrocycles

Non-enantiotropic atropisomers, also referred to as non-canonical atropisomers, are conformational isomers that arise from the concerted rotation of multiple σ bonds within macrocyclic frameworks possessing non-helical, conventional topologies. These atropisomers exhibit stereochemical behavior that differs fundamentally from classical axially chiral molecules, such as biaryl systems [91–96], in which chirality originates from restricted rotation around a single σ bond.

In 2016, Müllen's group first synthesized and separated two cyclohexa-1,3-pyrenylene **27** and **28** [97]. Experimental and theo-

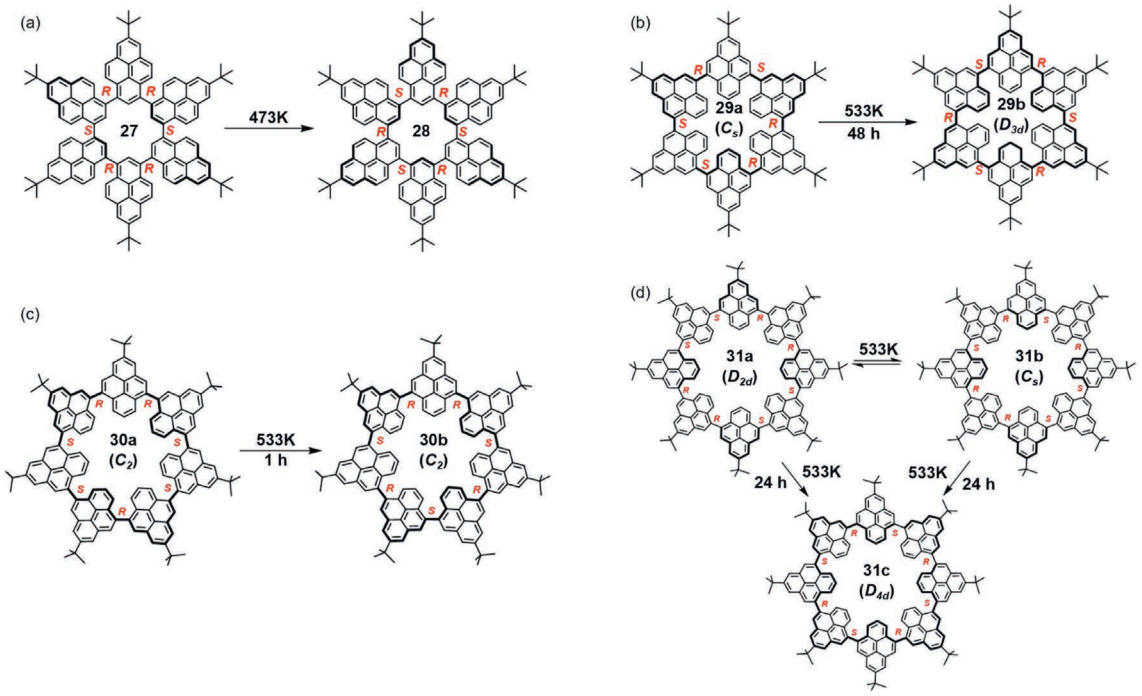


Fig. 15. Temperature-responsive conformational transitions of pyrene-containing macrocycles. (a) Isomer **27** converts to **28** upon heating at 473 K. (b) Isomer **29a** (C_s symmetry) transforms into **29b** (D_{3d} symmetry) after heating at 533 K for 48 h. (c) Isomer **30a** (C_2 symmetry) isomerizes to **30b** (C_2 symmetry) at 533 K within 1 h. (d) Isomers **31a** (D_{2d} symmetry) and **31b** (C_s symmetry) are interconvertible at 533 K, and both can further convert to **31c** (D_{4d} symmetry) after heating at 533 K for 24 h.

retical studies identified two plausible conformational structures, revealing that isomer **27** undergoes thermal conversion to the more thermodynamically stable isomer **28** upon heating to 473 K in [D8]sulfolane (Fig. 15a). However, the absence of comprehensive NMR and spectroscopic studies has limited the understanding of their dynamic behavior.

In 2023, Aratani, Yamada, and colleagues reported a series of [*n*]Cyclo-4,10-pyrenylenes (**29** ($n=6$), **30** ($n=7$), and **31** ($n=8$)) (Figs. 15b-d) [98]. They systematically investigated the atropisomeric distribution and conformational interconversion mechanisms in macrocycles of different sizes and refined NMR and spectroscopic characterization, providing deeper insight into their structural dynamics.

In 2018, Herges, Durola, and colleagues synthesized chiral non-enantiotropic triple helicene macrocycles **32a** (C_s symmetry) and **32b** (D_3 symmetry) from a common precursor molecule (Fig. 16a) [99]. UV-visible absorption spectroscopy revealed a significantly higher molar absorption coefficient relative to the [5]helicene core, while the atropisomers exhibited similar absorption peak profiles (Fig. 15b).

In 2021, Sato and Isobe synthesized [6]cyclo[4]helicenylenes ([6]CH) [100]. Four conformations (**33a–d**) were identified through HPLC separation and X-ray single-crystal diffraction, among which **33c** and **33d** were enantiomeric pairs (Fig. 17). Upon heating the isomer mixture to 473 K, the thermodynamically favored atropisomer **33a** was obtained in 12 % yield.

However, the kinetics of isomer transformation remained unexamined in the aforementioned studies. Furthermore, variations in the supramolecular chemistry of atropisomers were not investigated.

Since 2019, Gong's group has systematically investigated the atropisomerism of cyclo*meta*-phenylenes (CMPs). In 2019, they reported two atropisomers, **34** (C_s symmetry) and **35** (D_{4d} symmetry), of the novel all-hydrocarbon macrocycle cyclo[8](1,3-(4,6-dimethyl)benzene) (**CDMB-8**) and demonstrated complete conversion of **34** to **35** at 573 K (Fig. 18a) [101].

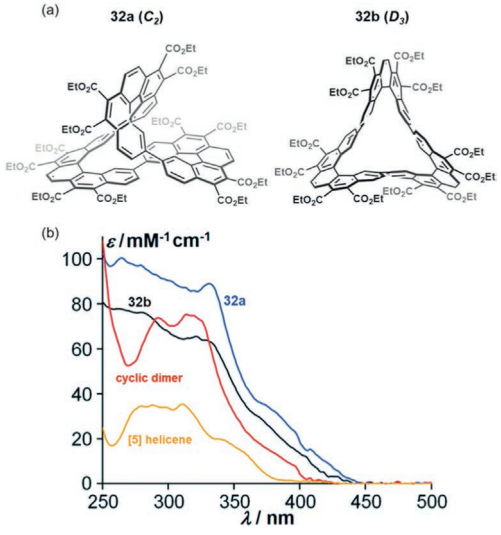


Fig. 16. (a) Structures of isomers **32a** (C_2 symmetry) and **32b** (D_3 symmetry). (b) Absorption spectra of a single [5]helicene tetraester (yellow), the corresponding cyclic dimer (red), and isomers **32a** (blue) and **32b** (black). Reproduced with permission [99]. Copyright 2018, The Royal Society of Chemistry.

In 2023, the group synthesized the pyridine-substituted cyclo[8](1,3-(4,6-dimethyl)benzene derivative **CP4**, which exists in three rigid atropisomeric forms: **36** (C_{4v} symmetry), **37** (C_s' symmetry), and **38** (C_s symmetry) [102]. NMR studies revealed that these atropisomers undergo reversible or irreversible interconversion under temperature regulation (Fig. 18b). Further theoretical calculations confirmed that these conformational transitions proceed *via* well-defined transition states.

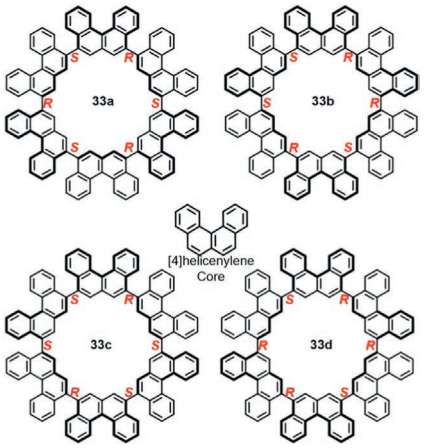


Fig. 17. Four atropisomers **33a-d** of [6]cyclo[4]helicenylenes ([6]CH).

Building on these findings, in 2024, the group synthesized an ester-substituted cyclo[8]-*meta*-phenylenes derivative, **OC-4** [103]. By tuning the reaction conditions, they selectively obtained two rigid atropisomers, **39** (C_{2v} symmetry) and **40** (C_{4v} symmetry). During thermodynamic investigations, they captured the conversion intermediate **41** (C_s symmetry) and found that the activation energy for atropisomerization was significantly reduced through this intermediate, enabling interconversion between atropisomers. Furthermore, *via* controlled chemical modifications, the group achieved efficient conversion from the most thermodynamically stable state **40** to the metastable state **39** and **41** (Fig. 18c).

Based on previous exploration of **CP4**, a cyclo[8]-*meta*-phenylenes derivative, they recently reported that **CP2**, modified with two pyridine substituents, is similar to **CP4** and also features three rigid atropisomers: **42** (C_s symmetry), **43** (C_1 symmetry), and **44** (C_{2v} symmetry) [104]. However, in contrast to the isomer transformation of **CP4**, NMR studies of **CP2** revealed that its atropisomers can interconvert through an intermediate, **45** (C_s' symmetry) (Fig. 18d). Thermal transformation experiments and theoretical calculations indicated that the intermediate process of **CP2** has a lower transition energy barrier compared to the transition state process of **CP4**. As a result, conformational transformation in **CP2** can occur at a relatively low temperature (393 K). These studies offer new strategies for optimizing stimulus-responsive behavior in atropisomeric macrocycles.

The distinct properties of atropisomers enabled the development of stimuli-responsive supramolecular self-assemblies with potential applications. The atropisomers **34** and **35**, reported by Gong's group, exhibited distinct host-guest interactions. Notably, **35** functions as a fullerene acceptor, facilitating the separation and purification of fullerenes from fullerene mixtures or carbon soot extracts, whereas **34** lacked these capabilities (Fig. 19a) [101]. In 2021, they synthesized a self-assembled multicomponent capsule structure, (((**35**)$_3$⊃(Cora)$_2$)⊃I_2) [105], in cyclohexane *via* the synergistic interactions between **35**, corannulene (Cora), and I_2 (Fig. 19b). Within this capsule, I_2 was encapsulated inside the (**35**)$_3$⊃(Cora)$_2$) shell, exhibiting remarkable stability. No evidence of I_2 escape was observed, even at elevated temperatures (up to 418 K). Similarly, the encapsulated I_2 remained unreactive toward alkaline and reductive aqueous solutions, such as saturated NaOH or $Na_2S_2O_3$. They propose that this multicomponent supramolecular structure offers a promising strategy for the encapsulation and stabilization of small high-energy molecules and reactive intermediates.

For the development of stimulus-responsive materials, **35** and a series of guest molecules (*e.g.*, perylene) can form fluorescent host-guest complexes [106,107]. By varying the solvent environment, these materials undergo transitions between co-crystalline,

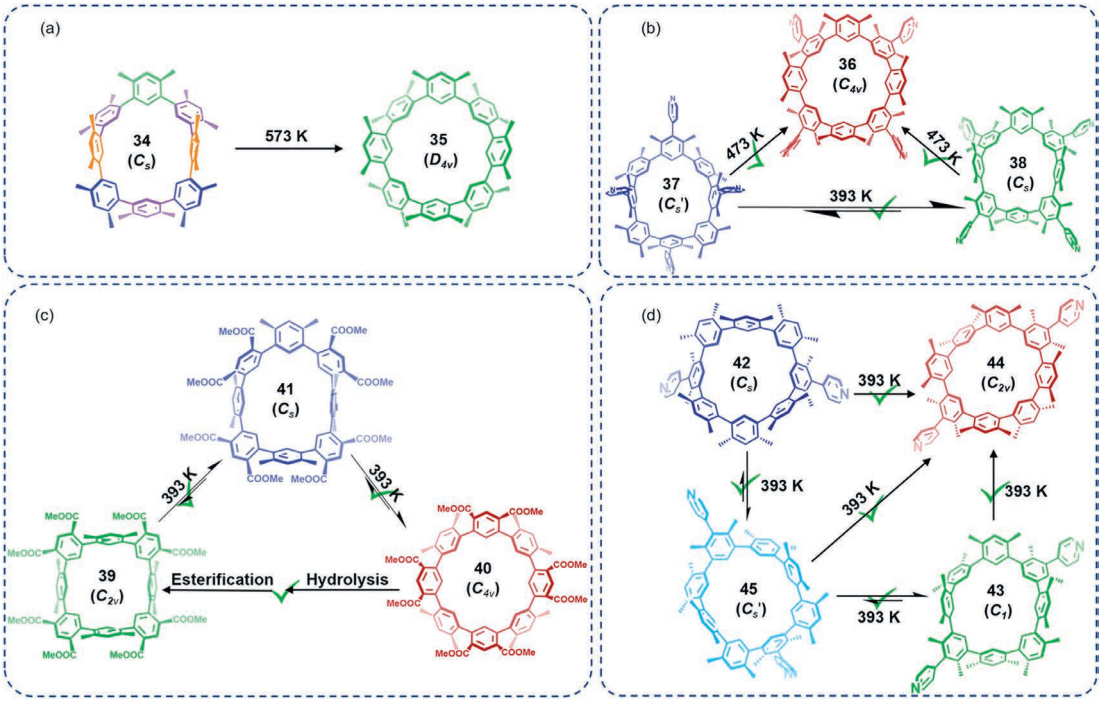


Fig. 18. (a) Thermal annealing achieves quantitative conversion of isomer **34** (C_s symmetry) to **35** (D_{4d} symmetry) at 573 K. (b) Schematic diagram of the reversible conversion of isomers **37** (C_s' symmetry) and **38** (C_s symmetry) at 393 K, and the quantitative conversion of isomers **37** (C_s' symmetry) and **38** (C_s symmetry) to **36** (C_{4v} symmetry) at 473 K. (c) Schematic diagram of the interconversion between isomers **39** (C_{2v} symmetry), **40** (C_{4v} symmetry) and intermediate **41** (C_s symmetry) at 393 K, and the efficient conversion of **40** (C_{4v} symmetry) to **39** (C_{2v} symmetry) under chemical reaction. (d) Schematic diagram of the interconversion between isomers **42** (C_s symmetry), **43** (C_1 symmetry), **44** (C_{2v} symmetry) and intermediate **45** (C_s' symmetry) at 393 K.

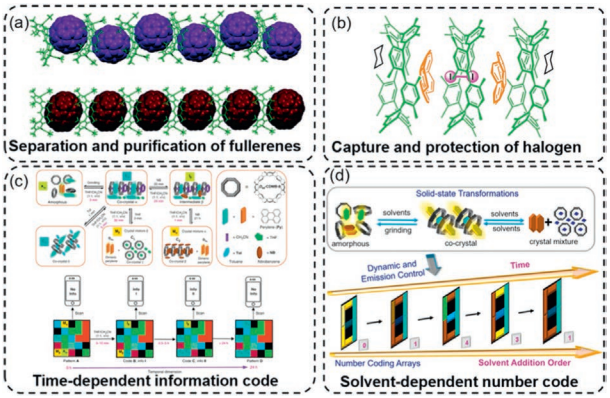


Fig. 19. (a) Separation and purification of fullerenes using **35**. (b) Emergent self-assembly of a multicomponent capsule structure (((**35**)$_3$⊃(Cora)$_2$)⊃I_2) in cyclohexane through the synergistic interaction between **35**, corannulene (Cora), and I_2. (c) Schematic diagram of the time-dependent dynamic 4D code system. (d) Specific number coding arrays. Reproduced with permission from [101,105–107]. Copyright 2019, The Royal Society of Chemistry; Copyright 2020, The Author(s); Copyright 2021, American Chemical Society; Copyright 2023, American Chemical Society.

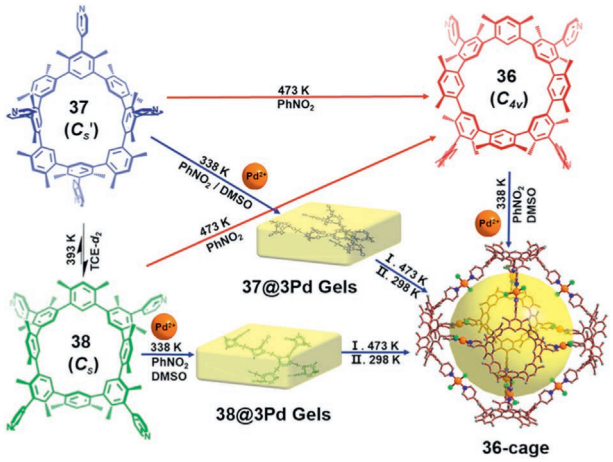


Fig. 20. Schematic diagram illustrating the heating regulation from macrocycle to further metal–organic cage assembly *via* both stepwise and *in situ* pathways. Isomers **37** and **38** coordinate with Pd^{2+} to form gels at temperatures below 338 K, which can be converted into metal–organic molecular cages upon heating at 473 K. The coordination of **36** with Pd^{2+} at 338 K directly forms the same cage, **36-cage**. Reproduced with permission [102]. Copyright 2023, The Author(s).

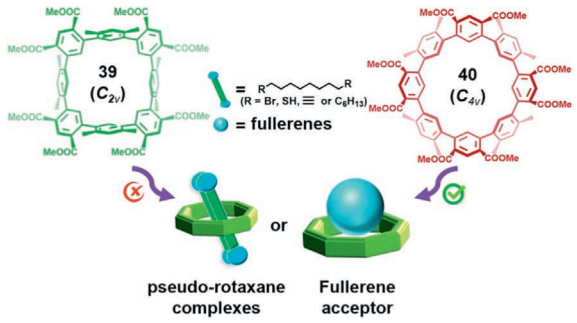


Fig. 21. Schematic diagram of complexes formed by **40** with linear guests or fullerenes, which can be used in fullerene separation and the construction of pseudo-rotaxane complexes. Reproduced with permission [103]. Copyright 2024, The Author(s).

crystalline mixture, and amorphous states. These phase transformations induce fluorescence changes with distinct time-dependent behaviors. These tunable fluorescence properties enable the creation of a time-dependent dynamic 4D code system (Fig. 19c) and specific number coding arrays (Fig. 19d), facilitating dynamic information encoding and automated optical reading. This system holds potential applications in gas-induced fluorescence sensing, high-density information storage, and *anti*-counterfeiting technologies.

Extending beyond individual molecular behavior, atropisomerism can also govern supramolecular self-assembly. In 2023, they elucidated the conformational interconversion of **CP4** atropisomers and investigated their supramolecular properties. The studies revealed that distinct atropisomers assemble into structurally unique Pd^{2+}-coordinated systems. X-ray single-crystal diffraction confirmed that atropisomers **37** (C_s' symmetry) and **38** (C_s symmetry) form network Pd^{2+}-coordinated assemblies, resulting in yellow gels (**37**@3Pd and **38**@3Pd). In contrast, atropisomer **36** (C_{4v} symmetry) assembled into a three-dimensional Pd^{2+}-coordinated cage structure (**36-cage**). Thermal annealing enabled precise control over macrocyclic atropisomer structures, allowing modulation of the self-assembly process and facilitating the synthesis of nanoscale metal-organic cages (Fig. 20) [102].

In 2024, they reported **OC-4**, displaying supramolecular behavior analogous to **CDMB-8**. Atropisomer **40** (C_{4v} symmetry), with higher molecular symmetry, exhibited enhanced host-guest interactions compared to atropisomer **39** (C_{2v} symmetry). X-ray single-crystal diffraction confirmed that **40** readily forms host-guest complexes with linear molecules and fullerenes (Fig. 21), demonstrating potential applications in fullerene separation and *pseudo*-rotaxane assembly [103].

In 2025, they reported the synthesis of **CP2**, which exhibits supramolecular behavior similar to **CP4**. The metastable isomers **42** (C_s symmetry) and **43** (C_1 symmetry), as well as the thermodynamically stable **44** (C_{2v} symmetry), independently react with Pd^{2+} in the presence of 1,4-dioxane to yield M_2L_2 rectangular molecular cages, labeled **A** or **B**, respectively. In contrast, replacing 1,4-dioxane with 1,1′,2,2′-tetrachloroethane leads to the formation of a unique M_3L_3 hexagonal molecular cage (**C**) from isomer **44** (C_{2v} symmetry). Notably, solvent exchange enables the reversible transformation between M_2L_2 cage **B** and M_3L_3 cage **C**. Furthermore, under the cooperative effects of temperature variation and solvent changes, M_2L_2 cage **A** can transition into either cage **B** or cage **C**, enabling a multipathway self-assembly system (Fig. 22). This multipathway self-assembly system offers a strategic approach for precisely controlling the formation of smart materials [104].

In 2020, Jasti's group developed StrainViz, a computational method that correlates strain energy with molecular reactivity [108]. This approach enables the localization and quantification of strain, aiding the prediction of atropisomer formation and serving as a valuable tool in atropisomer research (Fig. 23).

In 2022, Wu's group reported the synthesis of trimeric macrocycles *trans*-**46** and *cis*-**47** [109]. These atropisomeric structures displayed distinct aromatic characteristics and open-shell radical properties across various oxidation states. Oxidation by $AgSbF_6$ readily yielded the corresponding dications, producing **46**$^{2+}$·2SbF_6^- and **47**$^{2+}$·2SbF_6^-, respectively. Both experimental and theoretical analyses revealed that these dications exhibited distinct degrees of electronic coupling, with **46**$^{2+}$·2SbF_6^- adopting a singlet ground state, whereas **47**$^{2+}$·2SbF_6^- stabilized a triplet state to relieve strain. Notably, **46**$^{2+}$·2SbF_6^- demonstrated pronounced global antiaromaticity, while **47**$^{2+}$·2SbF_6^- exhibited no global aromaticity (Fig. 24). This study further enriched the current understanding of aromaticity in conjugated molecules, offering new insights into their electronic structures and stability.

In 2022, Cai and colleagues reported the synthesis of non-enantiotropic atropisomers **48a** and **48b**, which both exhibited bright blue fluorescence with a fluorescence quantum yield (Φ_F) of

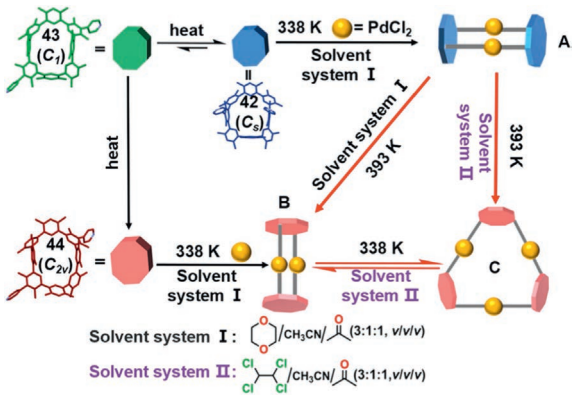


Fig. 22. Schematic diagram illustrating the temperature-induced interconversion among the three atropisomers enables the selective formation of distinct molecular cages. Reproduced with permission [104]. Copyright 2025, The Author(s). Published by PNAS.

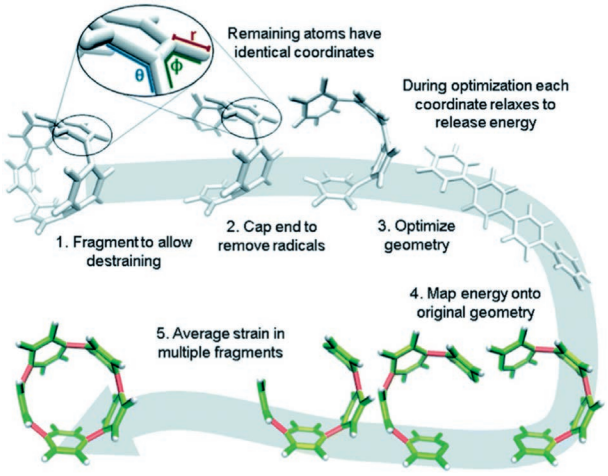


Fig. 23. Workflow for strain analysis. The coordinates in each molecular fragment relax to release strain energy, which is quantified per coordinate (r: bond length, q: angle, f: torsional angle). Copied with permission [108]. Copyright 2020, The Royal Society of Chemistry.

53 % (Fig. 25a) [59]. To explore the conformational interconversion between these atropisomers, variable-temperature ^{1}H NMR spectroscopy was employed. Upon heating to 90 °C for 2 h, a dynamic equilibrium was established, resulting in a 1:1 mixture of **48a** and **48b** (Fig. 25b). This molecular design strategy facilitates the simultaneous generation of enantiomers and diastereomers, enabling the comparative study of host–guest recognition across distinct conformational states.

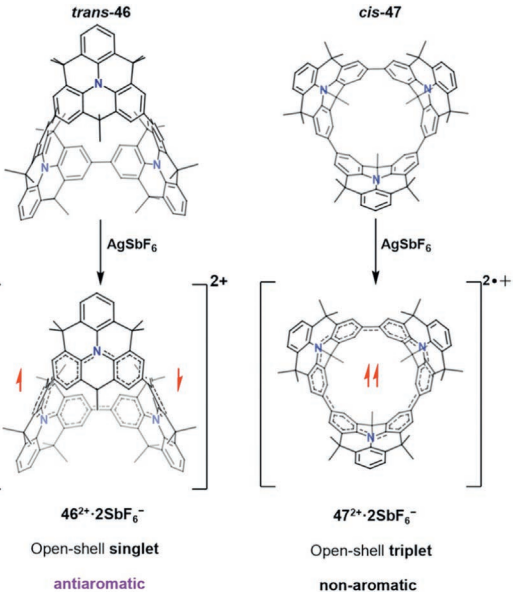


Fig. 24. The structure of trimeric macrocycles *trans*-**46** and *cis*-**47**, and their respective cations $\mathbf{46}^{2+}$·$2SbF_6^-$ and $\mathbf{47}^{2+}$·$2SbF_6^-$. The red arrows indicate the spins. The spin ground states and (*anti*) aromaticity of individual macrocycles are summarized below the structures.

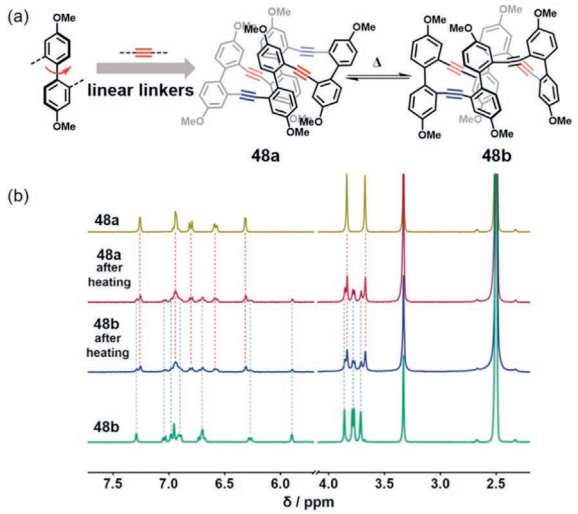


Fig. 25. (a) Synthetic strategy for macrocycles **48a** and **48b**. (b) ^{1}H NMR spectra (400 MHz, DMSO–d_6, 298 K) of **48a** and **48b** (1.0 mmol/L): spectra shown for pure **48a**, pure **48b**, and samples of each compound after heating at 90 °C for 2 h and rapidly cooling to 298 K. The spectra indicate that both macrocycles undergo thermally induced conformational interconversion, reaching an equilibrium mixture containing approximately equal amounts of **48a** and **48b** Reproduced with permission [59]. Copyright 2022, American Chemical Society.

4. Conclusion and outlook

In the past decade, enantiotropic atropisomers of carbon-rich cycloarenes and their macrocyclic derivatives have seen significant advancements. These atropisomers adopt distinct topological structures, leading to diverse properties in spatial functional site distribution, electronic configurations, and energy gaps. Such variations contribute to differences in chiroptical responses and host-guest recognition behaviors. This progress has provided new strategies for tuning the structures and properties of macrocycles and for designing novel carbon-rich materials.

In parallel, non-enantiotropic atropisomers of carbon-rich cycloarenes have gained increasing research interest due to their distinct conformations and associated physicochemical properties. However, existing studies have primarily centered on the synthesis of molecular frameworks and fundamental physicochemical characterization. Investigations into their atropisomeric behavior remain in an early stage, with challenges persisting in their selective synthesis. The mechanistic understanding of their interconversion is still underexplored, and precise control strategies have yet to be established. Furthermore, their potential applications in supramolecular chemistry remain largely unexplored.

Future efforts should prioritize the precise construction of enantiopure atropisomers with enhanced efficiency, selectivity, and scalability. Integrating experimental insights with theoretical modeling, we aim to systematically elucidate atropisomerization mech-

anisms and governing principles. Additionally, developing predictive theoretical frameworks for material behavior will facilitate the transition from fundamental research to real-world applications.

Finally, by leveraging atropisomerism, we aim to integrate additional molecular components to design stimulus-responsive supramolecular self-assembled materials. Establishing guiding principles for their formation will enable the exploration of their applicability in smart devices, biomedical technologies, energy systems, and environmental remediation.

Declaration of competing interest

The authors declare that they have no known competing financial interests or personal relationships that could have appeared to influence the work reported in this paper.

CRediT authorship contribution statement

Ke-Lin Zhu: Writing – original draft, Investigation, Data curation. **Zhi-Ao Li:** Supervision. **Jiaqi Liang:** Supervision. **Yong He:** Writing – review & editing. **Han-Yuan Gong:** Writing – review & editing, Supervision, Funding acquisition.

Acknowledgment

H.-Y. Gong is grateful to the National Natural Science Foundation of China (No. 92156009) for financial Support.

References

[1] M. Iyoda, J. Yamakawa, M.J. Rahman, Angew. Chem. Int. Ed. 50 (2011) 10522–10553.
[2] Y. Segawa, A. Yagi, K. Matsui, K. Itami, Angew. Chem. Int. Ed. 55 (2016) 5136–5158.
[3] K. Kaiser, L.M. Scriven, F. Schulz, et al., Science 365 (2019) 1299–1301.
[4] Z. Sun, K. Ikemoto, T.M. Fukunaga, et al., Science 363 (2019) 151–155.
[5] H. Chen, S. Gui, Y. Zhang, Z. Liu, Q. Miao, CCS Chem. 3 (2021) 613–619.
[6] K.Y. Cheung, K. Watanabe, Y. Segawa, K. Itami, Nat. Chem. 13 (2021) 255–259.
[7] T.H. Shi, M.X. Wang, CCS Chem. 3 (2021) 916–931.
[8] C. Zong, M.J. Wu, J.Z. Qin, A.J. Link, J. Am. Chem. Soc. 139 (2017) 10403–10409.
[9] P.J. Canfield, I.M. Blake, Z.L. Cai, et al., Nat. Chem. 10 (2018) 615–624.
[10] K. Zhu, G. Baggi, S.J. Loeb, Nat. Chem. 10 (2018) 625–630.
[11] X.H. Zhou, X. Zhang, Y.R. Song, et al., Angew. Chem. Int. Ed. 64 (2025) e202415190.
[12] T.R. Luan, C. Sun, Y.L. Tian, et al., Nat. Commun. 16 (2025) 2370.
[13] Y.E. Zhang, Y. Jiang, Y. Zhang, et al., Chin. Chem. Lett. 36 (2025) 111201.
[14] O. Shalev, S.E. Biali, Org. Lett. 20 (2018) 3390–3393.
[15] N. Li, J.J. Liu, J.W. Sun, et al., Green Chem. 22 (2020) 5325–5332.
[16] N.A. Grosso-Giordano, C. Schroeder, L. Xu, et al., Angew. Chem. Int. Ed. 60 (2021) 10239–10246.
[17] H.J.S. Banks, J.W.A. Frese, M.R.J. Elsegood, C. Redshaw, Chem. Commun. 60 (2024) 304–307.
[18] S. Mosca, Y. Yu, J. Rebek Jr., Nat. Protoc. 11 (2016) 1371–1387.
[19] N.W. Wu, I.D. Petsalakis, G. Theodorakopoulos, Y. Yu, J. Rebek Jr., Angew. Chem. Int. Ed. 57 (2018) 15091–15095.
[20] M. Petroselli, V. Angamuthu, F.U. Rahman, et al., J. Am. Chem. Soc. 142 (2020) 2396–2403.
[21] T.R. Li, G. Piccini, K. Tiefenbacher, J. Am. Chem. Soc. 145 (2023) 4294–4303.
[22] Y. Peng, S. Tong, Y. Zhang, M.X. Wang, Angew. Chem. Int. Ed. 62 (2023) e202302646.
[23] J. Yao, W. Wu, W. Liang, et al., Angew. Chem. Int. Ed. 56 (2017) 6869–6873.
[24] H. Liang, B. Hua, F. Xu, et al., J. Am. Chem. Soc. 142 (2020) 19772–19778.
[25] C. Xiao, W. Wu, W. Liang, et al., Angew. Chem. Int. Ed. 59 (2020) 8094–8098.
[26] S. Ohtani, S. Akine, K. Kato, et al., J. Am. Chem. Soc. 146 (2024) 4695–4703.
[27] T.H. Shi, S. Akine, S. Ohtani, K. Kato, T. Ogoshi, Angew. Chem. Int. Ed. 63 (2024) e202318268.
[28] M.Y. Zhao, Q.H. Guo, M.X. Wang, Org. Chem. Front. 5 (2018) 760–764.
[29] S. Tong, J.T. Li, D.D. Liang, et al., J. Am. Chem. Soc. 142 (2020) 14432–14436.
[30] Y. Gao, J. Guo, Y. Lai, et al., Angew. Chem. Int. Ed. 63 (2024) e202315691.
[31] X.N. Han, Y. Han, C.F. Chen, J. Am. Chem. Soc. 142 (2020) 8262–8269.
[32] X. Wang, F. Jia, L.P. Yang, H. Zhou, W. Jiang, Chem. Soc. Rev. 49 (2020) 4176–4188.
[33] X.N. Han, Y. Han, C.F. Chen, Nat. Commun. 12 (2021) 6378.
[34] Y.Y. Fan, D. Chen, Z.A. Huang, et al., Nat. Commun. 9 (2018) 3037.
[35] S. Hitosugi, W. Nakanishi, T. Yamasaki, H. Isobe, Nat. Commun. 2 (2011) 492.
[36] S. Hitosugi, T. Yamasaki, H. Isobe, J. Am. Chem. Soc. 134 (2012) 12442–12445.
[37] T. Matsuno, S. Kamata, S. Hitosugi, H. Isobe, Chem. Sci. 4 (2013) 3179–3183.
[38] K. Kogashi, T. Matsuno, S. Sato, H. Isobe, Angew. Chem. Int. Ed. 58 (2019) 7385–7389.
[39] H. Isobe, S. Hitosugi, T. Yamasaki, R. Iizuka, Chem. Sci. 4 (2013) 1293–1297.
[40] T. Matsuno, M. Someya, S. Sato, S. Maeda, H. Isobe, Angew. Chem. Int. Ed. 59 (2020) 14570–14576.
[41] T. Matsuno, S. Sato, R. Iizuka, H. Isobe, Chem. Sci. 6 (2015) 909–916.
[42] T. Matsuno, S. Sato, A. Yokoyama, S. Kamata, H. Isobe, Angew. Chem. Int. Ed. 55 (2016) 15339–15343.
[43] T. Matsuno, M. Fujita, K. Fukunaga, S. Sato, H. Isobe, Nat. Commun. 9 (2018) 3779.
[44] T. Matsuno, K. Fukunaga, S. Sato, H. Isobe, Angew. Chem. Int. Ed. 58 (2019) 12170–12174.
[45] T. Matsuno, S. Kamata, S. Sato, et al., Angew. Chem. Int. Ed. 56 (2017) 15020–15024.
[46] S. Sato, T. Yamasaki, H. Isobe, Proc. Natl. Acad. Sci. U. S. A. 111 (2014) 8374–8379.
[47] H. Isobe, K. Nakamura, S. Hitosugi, et al., Chem. Sci. 6 (2015) 2746–2753.
[48] T. Matsuno, Y. Nakai, S. Sato, Y. Maniwa, H. Isobe, Nat. Commun. 9 (2018) 1907.
[49] S. Terasaki, Y. Kotani, R. Katsuno, et al., Angew. Chem. Int. Ed. 63 (2024) e202406502.
[50] T. Matsuno, S. Terasaki, K. Kogashi, R. Katsuno, H. Isobe, Nat. Commun. 12 (2021) 5062.
[51] Y. Kotani, R. Katsuno, K. Sambe, et al., Angew. Chem. Int. Ed. 64 (2025) e202425308.
[52] H. Omachi, Y. Segawa, K. Itami, Org. Lett. 13 (2011) 2480–2483.
[53] J. Wang, G. Zhuang, Q. Huang, et al., Chem. Commun. 55 (2019) 9456–9459.
[54] J. Wang, H. Shi, S. Wang, et al., Chem. Eur. J. 28 (2022) e202103828.
[55] J. Wang, G. Zhuang, M. Chen, et al., Angew. Chem. Int. Ed. 59 (2020) 1619–1626.
[56] D. Wassy, M. Hermann, J.S. Wossner, et al., Chem. Sci. 12 (2021) 10150–10158.
[57] M. Hermann, D. Wassy, J. Kohn, et al., Angew. Chem. Int. Ed. 60 (2021) 10680–10689.
[58] Y. Yu, Y. Hu, C. Ning, et al., Angew. Chem. Int. Ed. 63 (2024) e202407034.
[59] H. Han, R. Fu, R. Wang, et al., J. Am. Chem. Soc. 144 (2022) 20351–20362.
[60] R. Fu, Q.Y. Zhao, H. Han, et al., Angew. Chem. Int. Ed. 62 (2023) e202315990.
[61] R. Wang, L.B. Jing, J.Y. Deng, et al., CCS Chem. (2025), doi:10.31635/ccschem.025.202505572.
[62] X. Zhang, H. Shi, G. Zhuang, et al., Angew. Chem. Int. Ed. 60 (2021) 17368–17372.
[63] X. Zhang, H. Liu, G. Zhuang, S. Yang, P. Du, Nat. Commun. 13 (2022) 3543.
[64] Y. Zhang, D. Yang, S.H. Pun, H. Chen, Q. Miao, Precis. Chem. 1 (2023) 107–111.
[65] G. Li, L.L. Mao, J.N. Gao, et al., Angew. Chem. Int. Ed. 64 (2025) e202419435.
[66] Q. Huang, G. Zhuang, M. Zhang, et al., J. Am. Chem. Soc. 141 (2019) 18938–18943.
[67] T.M. Fukunaga, T. Kato, K. Ikemoto, H. Isobe, Proc. Natl. Acad. Sci. U. S. A. 119 (2022) e2120160119.
[68] Y.J. Shen, K.L. Zhu, J.Q. Liang, X. Sun, H.Y. Gong, J. Mater. Chem. C 11 (2023) 4267–4287.
[69] Y. Segawa, T. Watanabe, K. Yamanoue, et al., Nat. Synth. 1 (2022) 535–541.
[70] L. Ye, C. Hu, D. Yang, et al., J. Am. Chem. Soc. 147 (2025) 17795–17803.
[71] R. Herges, M. Deichmann, T. Wakita, Y. Okamoto, Angew. Chem. Int. Ed. 42 (2003) 1170–1172.
[72] L.H. Wang, N. Hayase, H. Sugiyama, et al., Angew. Chem. Int. Ed. 59 (2020) 17951–17957.
[73] S. Castro-Fernandez, R. Yang, A.P. Garcia, et al., Chem. Eur. J. 23 (2017) 11747–11751.
[74] A. Ozcelik, D. Aranda, S. Gil-Guerrero, et al., Chem. Eur. J. 26 (2020) 17342–17349.
[75] K. Zhu, K. Kamochi, T. Kodama, M. Tobisu, T. Amaya, Chem. Sci. 11 (2020) 9604–9610.
[76] Y. Fan, J. He, L. Liu, et al., Angew. Chem. Int. Ed. 62 (2023) e202304623.
[77] J. He, Y. Fan, Z. Lian, et al., Adv. Optical Mater. 12 (2023) 2302221.
[78] J. He, M.H. Yu, Z. Lian, et al., Chem. Sci. 14 (2023) 4426–4433.
[79] S. Guo, L. Liu, F. Su, et al., JACS Au 4 (2024) 402–410.
[80] L. Tong, R.R. Gattass, J.B. Ashcom, et al., Nature 426 (2003) 816–819.
[81] G.R. Schaller, F. Topic, K. Rissanen, et al., Nat. Chem. 6 (2014) 608–613.
[82] S. Miguez-Lago, A.L. Llamas-Saiz, M. Magdalena Cid, J.L. Alonso-Gomez, Chem. Eur. J. 21 (2015) 18085–18088.
[83] Y. Segawa, M. Kuwayama, Y. Hijikata, et al., Science 365 (2019) 272–276.
[84] X. Jiang, J.D. Laffoon, D. Chen, et al., J. Am. Chem. Soc. 142 (2020) 6493–6498.
[85] J. Zhang, H. Chen, X. Qin, et al., Org. Lett. 24 (2022) 9463–9467.
[86] W. Fan, T.M. Fukunaga, S. Wu, et al., Nat. Synth. 2 (2023) 880–887.
[87] L. Zhan, H. Xiao, J.N. Gao, H. Cong, Org. Chem. Front. 10 (2023) 5395–5401.
[88] W. Fan, T. Matsuno, Y. Han, et al., J. Am. Chem. Soc. 143 (2021) 15924–15929.
[89] Q. Zhou, X. Hou, J. Wang, et al., Angew. Chem. Int. Ed. 62 (2023) e202302266.
[90] A. Bu, Y. Zhao, H. Xiao, et al., Angew. Chem. Int. Ed. 61 (2022) e202209449.
[91] A. Bu, J.N. Gao, Y. Chen, et al., Angew. Chem. Int. Ed. 63 (2024) e202401838.
[92] L. Pu, Chem. Rev. 98 (1998) 2405–2494.
[93] Y. Chen, S. Yekta, A.K. Yudin, Chem. Rev. 103 (2003) 3155–3212.
[94] L. Pu, Acc. Chem. Res. 50 (2017) 1032–1040.
[95] L. Pu, Angew. Chem. Int. Ed. 59 (2020) 21814–21828.
[96] M. Kondo, K. Nakamura, C.G. Krishnan, et al., ACS Catal. 11 (2021) 1863–1867.
[97] D. Lorbach, A. Keerthi, T.M. Figueira-Duarte, et al., Angew. Chem. Int. Ed. 55 (2016) 418–421.

[98] R. Kurosaki, H. Morimoto, K. Matsuo, et al., Chem. Eur. J. 29 (2023) e202203848.
[99] G. Naulet, L. Sturm, A. Robert, et al., Chem. Sci. 9 (2018) 8930–8936.
[100] T. Matsuno, Y. Yang, Y. Nanjo, H. Isobe, S. Sato, Chem. Lett. 50 (2021) 110–112.
[101] Y.D. Yang, H.Y. Gong, Chem. Commun. 55 (2019) 3701–3704.
[102] J. Liang, S. Lu, Y. Yang, et al., Nat. Commun. 14 (2023) 8166.
[103] X. Sun, J.K. Bai, Y.D. Yang, et al., Nat. Commun. 15 (2024) 6559.
[104] J. Liang, L.J. Peng, K.L. Zhu, et al., Proc. Natl. Acad. Sci. U. S. A. 122 (2025) e2500357122.
[105] Y.D. Yang, X.L. Chen, J.L. Sessler, H.Y. Gong, J. Am. Chem. Soc. 143 (2021) 2315–2324.
[106] Y.D. Yang, X. Ji, Z.H. Lu, et al., Nat. Commun. 11 (2020) 77.
[107] Y.D. Yang, X.L. Chen, J. Liang, et al., J. Am. Chem. Soc. 145 (2023) 14010–14018.
[108] C.E. Colwell, T.W. Price, T. Stauch, R. Jasti, Chem. Sci. 11 (2020) 3923–3930.
[109] S. Wu, Y. Ni, Y. Han, et al., J. Am. Chem. Soc. 144 (2022) 23158–23167.